C. Hirose[1]†, D. Nakashima[2], C. Aoyama[3,4], and H. Watanabe[1]

[1]Faculty of Engineering Sciences, Kyushu University.

[2]Interdisciplinary Graduate School of Engineering Sciences, Kyushu University.

[3]Japan's Independent Institute Co., Ltd.

[4]Faculty of Marine Resources and Environment, Tokyo University of Marine Science and Technology.

Corresponding author: Chiyoko Hirose (Chiyoko_ikgy@kyudai.jp)

†Faculty of Engineering Sciences, Kyushu University, Kasuga-koen 6-1, Kasuga-shi, Fukuoka, 816-8580, Japan.

Key Points:

- Imaging data of methane bubbles obtained in natural gas seep sites and direct numerical simulations were provided.
- The statistical and stochastic features of the upwelling behavior of methane bubbles were reported based on quantitative image analysis.
- The differences between methane bubbles with and without hydrate formation were discussed in terms of velocity, size, and shape.

Abstract

In this study, we conducted a quantitative analysis of the behavior of ascending methane bubbles, which were filmed at two natural gas seep sites and reproduced by numerical simulations using two-dimensional motion analysis software. The targeted sites were located in the southwest and northeast of Sado Island at the eastern margin of the Sea of Japan, where methane bubbles with and without a methane hydrate (MH) layer were observed, respectively. The simulations comprising gas bubbles and MH bubbles spouting from a nozzle in the computational domain filled with pure water were generated to assess the validity of the image analysis for situ-data, while the numerical models and physical properties were utilized for current two-phase (gas-liquid) simulations. The rising velocity, size, circumference, circularity, and maximum diameter of methane bubbles were examined to understand the effects of the MH layer on the statistical and stochastic features of ascending methane bubbles. Based on the statistics of the aforementioned variables, gas bubbles had a higher rising velocity and smaller circularity than MH bubbles when the bubble sizes were identical. Furthermore, the stochastic analysis indicated that the circularity of the MH bubble was uniquely determined by the size of the bubble owing to the more rigid skin of the MH bubbles compared to that of the gas bubbles.

Plain Language Summary

Ocean surveys, which covered the eastern margin of the Sea of Japan, offshore Niigata prefecture, were conducted in June 2019 and November 2021. The target sea region has attracted remarkable attention owing to its numerous

methane plumes and extreme submarine methane seepage, which are considered the major sources of primary energy supply. By assuming that the collection of methane gas released from the seafloor is a sub-oceanic resource, it serves as a fundamental but essential process for understanding the behavior of methane bubbles released from the seafloor. However, there is very limited knowledge on the velocities, sizes, and shapes of methane bubbles with and without the methane hydrate (MH) layer on the bubble surfaces. Therefore, in this study, we quantitatively analyzed the unsteady ascending motion of methane bubbles, which were filmed at two natural gas seep sites and reproduced by numerical simulations using two-dimensional image analysis. Based on a comparison of the results, we further clarified the effects of the MH layer on the statistical and stochastic features of the motion and shape of the upwelling methane bubbles.

1 Introduction

Methane hydrate (MH) is an ice-like or sherbet-like substance comprising methane and water molecules. In recent years, the possible existence of a remarkable amount of MH within ocean sediments has been reported by numerous researchers worldwide (Lee, 2000; Roberts, 2001 ; Liu et al., 2006). As MH is well known as a potential energy resource, it has attracted growing attention, especially countries that need to improve their energy self-sufficiency, such as Japan. Notably, some research and development (R&D) projects on MH exploitation were launched in Japan. For example, according to the MH21 Research Consortium (Nagakubo et al., 2007), MH exists at the eastern Nankai Trough (Matsumoto et al., 2004), under the Sea of Japan offshore Niigata Prefecture (Aoyama and Matsumoto, 2009). Referring to previous reports, the methane plume (or the methane flare), which is a cluster of methane bubbles naturally spouting from the seabed, can be a good indicator of the shallow-type MH being more abundant than the pore-filling sand layer type in the Sea of Japan. By targeting the utilization of the shallow-type MH as a next-generation energy resource, methods for estimating the amount of MH from the methane plumes by acoustic observation have been proposed by Aoyama and Maeda (2021). Further, a capturing system for methane bubbles within the methane plumes is currently being developed under the national project launched in 2001 (National Institute of Advanced Industrial Science and Technology, 2019).

Knowledge on MH occurrence with interrelations among temperature, pressure, and composition is very limited (Knenvolden, 1993) owing to the following two main reasons. First, the composition of the bubbles in the liquid-gas-solid phases (i.e., seawater, methane gas, and MH) and the resultant physical properties are unavailable in most cases, despite thoughts that the gas seeping from the seabed is generally composed of methane mainly (Leifer et al., 2006; Wang et al., 2016). Second, the phase change of methane between the liquid, gas, and solid phases is associated with marked changes in temperature and pressure during the ascending process of moving from the sea bottom to the surface of the sea, resulting in the complexity of the motion and shape of methane bubbles characterized by distortion, adhesion, and dissociation. In short, fundamental studies on the

properties of the ascending behavior of methane bubbles (either covered with MH layer or not) are required for substantial and effective system designed to exploit methane bubbles. In addition, the development of numerical models to reasonably reproduce the behavior of ascending bubbles is inevitable for establishing a low-cost and highly efficient method to exploit methane bubbles spouting from the seabed.

Based on the aforementioned background, in this study, we statistically analyzed video images of unsteadily ascending methane bubbles, which were collected in ocean surveys and numerical simulations. Situ-filming was conducted at two sites in the eastern margin of the Sea of Japan, offshore Niigata Prefecture, by sending a remotely operated vehicle (ROV) to depths of 891.8 m and 153 m, to observe the MH bubbles and gas bubbles spouting from the seabed, respectively. In addition, direct numerical simulations (DNS), which reproduced the effect of an MH skin on the bubble surfaces using the value of the surface tension coefficient, were performed using the conditions of a validation study or the situ-site.

The physical quantities of the motion and shape of the methane bubbles, such as position, velocity, size, circularity, and circumference, were measured using a two-dimensional motion analysis software, which can track the trajectories of moving bubbles. Further, based on quantitative data, the stochastic properties and statistical features of ascending methane bubbles in surveys and simulations were discussed in detail. The obtained results can provide useful information for understanding the motion and shape of bubbles with and without a hydrate layer on their surface.

2 Research Methodology

2.1 Data Acquisition via Ocean Surveys

The image data analyzed in this study were collected from two ocean surveys conducted on June 9–13, 2019 and November 14–19, 2021. The target sea regions were Site-A and Site-B in Fig. 1, which belong to the eastern margin of the Sea of Japan, offshore Niigata prefecture. Site-A is located at a spur with a length of 8 km from north to south and 2 km from east to west, with a maximum depth of 850–940 m (Matsumoto et al., 2009). In contrast, Site-B is in the Mogami Trough and has a length of 10 km and a depth of 600–700 m (Inoue et al., 2011). The eastern margin of the Sea of Japan has attracted remarkable attention owing to its numerous methane plumes and extreme submarine methane seepage, which indicate the existence of shallow-type MH near the seafloor surface (Matsumoto, 2005, Matsumoto et al., 2009, Aoyama and Matsumoto, 2009).

As shown in Fig. 2, an ROV equipped with a high-definition color inspection camera (OE14-502, Kongsberg Maritime Ltd.) was sent to at a depth of 891.8 m at the seabed of Site-A and 153 m at that of Site-B to observe active methane gas seeps. Snapshots of clear-cut video images with a flame rate of 25 fps are shown in Fig. 3. At both sites, seeping methane gas was captured as

white objects rising from bottom to top in the images from the videos. As the methane bubbles at Site-A (Fig. 3 (a)) were filmed at approximately 1 m above seafloor (depth of 891.8 m), their release time can be estimated to be more than 7 s (based on the average vertical velocity at the lowest position in the analysis area, which is approximately 15 cm/s). Therefore, the bubbles at Site A were considered to be covered with a thin hydrate layer, with a release time of 10 s for fully hydrate-coated bubbles, as reported by Fu et al. (2021). The accumulated methane bubbles observed inside the flask in Fig. 3(a) support this observation. In contrast, the methane bubbles at Site-B (Fig. 3 (b)) were filmed at approximately 0.3 m above the seafloor at a depth of 153 m. Hence, the methane bubbles at Site-B are completely gas bubbles based on the hydrate stability conditions.

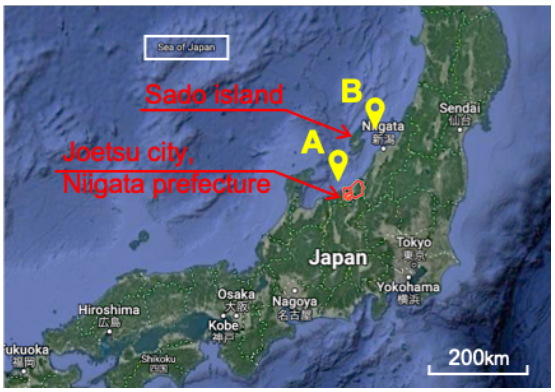

Figure 1. The location of the natural gas seep sites (reproduced from Google map). Site-A and Site-B are si

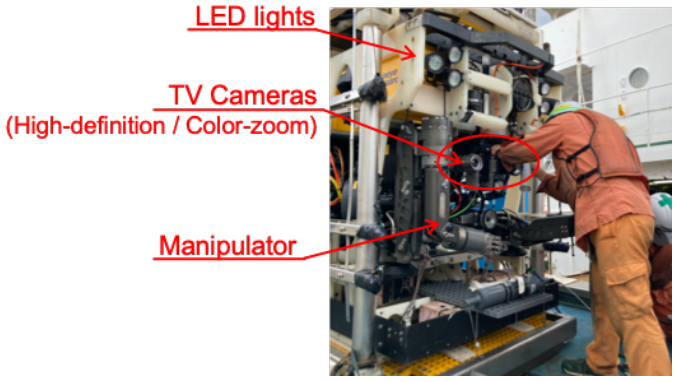

Figure 2. ROV stored at the tether management system (TMS), which enables ROV to operate at a larger r

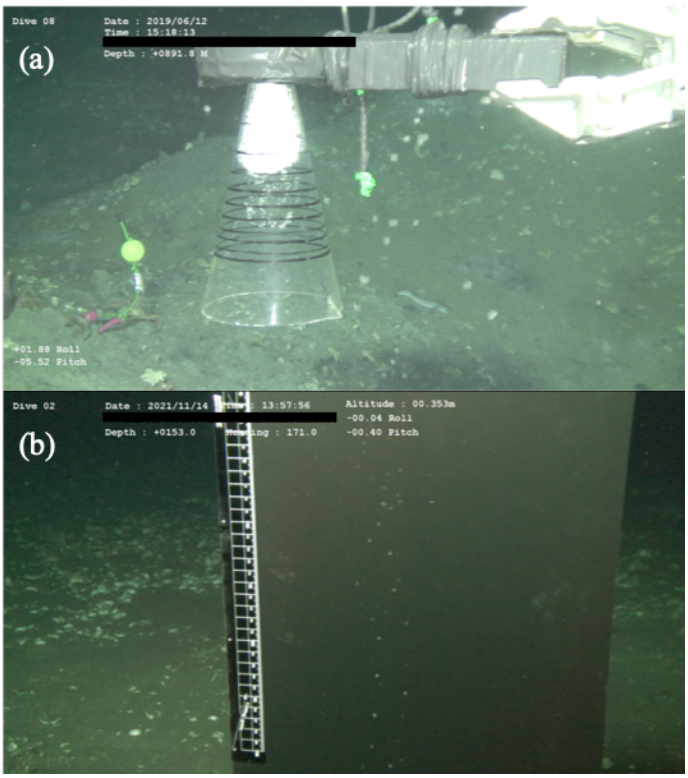

Figure 3. Snapshot of methane bubbles seeping from the seabed at (a) Site-A and (b) Site-B. The dive at Si

2.2 Data Acquisition via Numerical Simulations

In this study, direct numerical simulations (DNS) for an incompressible immiscible two-phase flow (liquid and gas) were performed using the general-purpose fluid analysis code, NuFD/FrontFlowRed, extended by Kyushu University (Watanabe et al., 2020). The visualized images obtained by simulations were compared with the in-situ video images to evaluate the reproducibility of the utilized numerical model for methane bubbles with and without a hydrate layer.

The schematics of the computational domain and boundary conditions are shown in Fig. 4. Methane gas was emitted to the domain field filled with water from the tip of the nozzle (corresponding to the inlet boundary), with a mass flux of Q m^3/s, as described in Table 1. The inner diameter of the nozzle was 2.27 mm, the grids were composed of a hexa-mesh, and the total number of mesh was approximately 9 million.

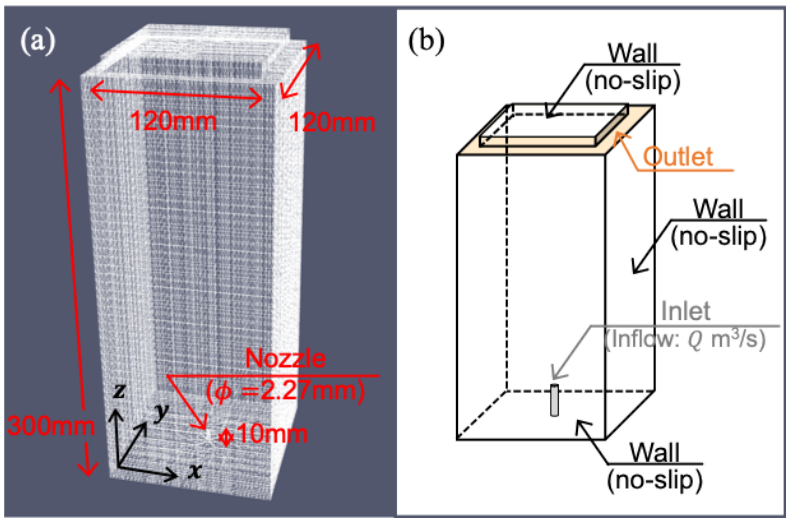

Figure 4. Simulation settings. (a) Computational domain and (b) boundary conditions.

Table 1. Simulation conditions and physical properties.

Case	Bubble state	Pressure	Temperature	Density (Water)	Density (Gas)	Viscosity (Water)	Viscosity (Gas)	Surface tension coefficient	Inflow rate
		P [MPa]	T [K]	ρ_L [kg/m^3]	ρ_G [kg/m^3]	μ_L [Pa·s]	μ_G [Pa·s]	σ [N/m]	Q [m^3/s]
	Gas					$\times 10^{-3}$	$\times 10^{-5}$		$\times 10^{-7}$
	&								
	MH								
	Gas					$\times 10^{-3}$	$\times 10^{-5}$		$\times 10^{-7}$
	Gas					$\times 10^{-3}$	$\times 10^{-5}$		$\times 10^{-6}$

The finite volume method was employed to discretize the governing equations, including the incompressible continuity (Eq. (1)) and Navier-Stokes equations (Eq. (2)),

$$\frac{\partial \rho u_i}{\partial x_i} = 0, \tag{1}$$

$$\frac{\partial \rho u_i}{\partial t} + \frac{\partial \rho u_i u_j}{\partial x_i} = -\frac{\partial p \delta_{ij}}{\partial x_j} - \frac{\partial}{\partial x_j}\left\{\mu\left(\frac{\partial u_i}{\partial x_j} + \frac{\partial u_j}{\partial x_i}\right)\right\} + \rho g_i + F_\sigma, \tag{2}$$

where is density [kg/m^3], u_i ($i = 1, 2, 3$ for u, v, w) denotes the velocity component [m/s] in x_i direction ($i = 1, 2, 3$ for x: horizontal, y: depth, z: vertical), is viscosity [Pa s], g_i is the gravitational acceleration in x_i direction [m/s^2], and F_σ represents the effect of the volumetric surface tension force, which is estimated using the continuum surface force (CSF) model (Brackbill et al., 1992). In the CSF model, F_σ was obtained using the following equation:

$$F_\sigma = \sigma \kappa \mathbf{n} \delta_s, \quad (3)$$

where σ is the surface tension coefficient [N/m], κ is the interface curvature, $\mathbf{n}$ is the normal vector at the interface, and δ_s is the Dirac delta function, which is equal to zero, except at the interface. The temporal and spatial differential terms in the governing equations were discretized using the Euler backward and second-order upwind schemes, respectively. For the pressure-velocity coupling, the SIMPLE procedure (Versteeg and Malalasekera, 1998) was employed.

As the immiscible fluid in the current simulation can be modelled as a set of two fluids (water and methane), the additional constative relations in ρ and μ are introduced in Eqs. (4) and (5),respectively:

$$\rho = \alpha \rho_L + (1 - \alpha) \rho_G, \quad (4)$$

$$\mu = \alpha \mu_L + (1 - \alpha) \mu_G, \quad (5)$$

where α is the volume fraction ranging from 0 to 1 and the subscripts of L and G indicate the liquid (background) and gas, respectively. Accordingly, the liquid is defined in cells where $\alpha = 1$, whereas the gas is defined in cells where $\alpha = 0$. If α is between 0 and 1, the cell is regarded to contain both fluids, which results in the identification of the location of the interface between the fluids. Assuming the incompressible conditions of the current simulation, α satisfies the advective relations expressed in Eqs. (6),

$$\frac{\partial \alpha}{\partial t} + u_j \frac{\partial \alpha}{\partial x_j} = 0. \quad (6)$$

This method is called the volume of fluid (VOF) method (Hirt and Nichols, 1981) and is widely used to simulate flows with moving interfaces. The total mass conservation of fluids can be maintained very well via the VOF method, which is an advantage; however, the interference normal and curvature are inaccurate as α in VOF is a step function, thereby serving as a limitation of the method. To avoid numerical errors related to the aforementioned weakness, the counter-gradient transport method provided by Weller (1993) was applied to the volume fraction equation (Eq. (6)) and Eq. (7) is obtained as follows:

$$\frac{\partial \alpha}{\partial t} + u_j \frac{\partial \alpha}{\partial x_j} + u_j \frac{\partial \alpha(1-\alpha)}{\partial x_j} = 0. \quad (7)$$

Here, the last term on the left-hand side represents the compressive term that can preserve the interface sharpness and account for the interface orientation and advection velocity. The discretization of the time derivation and the nonlinear convective term in Eq. (7) was performed using a high-resolution interface-capturing (HRIC) scheme (Muzaferija et al., 1998).

To the best of our knowledge, a consensus on how the fluid dynamics of MH bubbles can be reproduced using numerical simulation has yet to be reached among researchers. Therefore, in this study, the simulation data were validated with the experimental study conducted by Sato et al. (2013), who investigated the motion of a single MH bubble in a quiescent fluid. The detailed conditions and physical properties used in the simulations are listed in Table 1. The settings for Case-1, whose bubble state must be covered with the MH layer, follow those mentioned by Sato et al. (2013), while those for Case-2, whose settings are the same as Case-1, besides σ, which implies that the bubbles must be composed of methane gas alone, was employed to examine the difference in ascending behavior of bubbles depending on whether a hydrate layer exists on the bubble surface. Case-3, which employs the ambient conditions assumed to follow the filming location at Site-A, was simulated for comparison with in-situ video images at Site-A. As there were no data of σ for the methane bubbles on the seafloor at Site-A, the value of 0.756 N/m, which is the value for the water at conditions of 1 atm and 273.15 K, was applied to Case-3.

The simulations were performed using 36-core parallel computation on the ITO computer of Kyushu University (Fujitsu PRIMERGY CX2550/CX2560 M4). The physical time in each case was 10 s, with a time step of 2.5×10^{-5} s, which took approximately 108 node hours. The simulation data were sampled every 4.0×10^{-2} s corresponding to the frame rate of the video images obtained at Sites A and B. Based on the corrected data, the ascending bubbles are visualized as the iso-surface of the void ratio of 0.5, which can be recognized as the interface between the liquid (*i.e.*, water) and gas (*i.e.*, methane bubbles) in the two-phase flow simulation.

3. Methodology of Image Analysis

The behaviors of the ascending bubbles observed in ocean surveys and simulations were analyzed using the two-dimensional motion analysis software, Move-tr/2D Ver. 8.6 (Library Co., Ltd.), which can track the trajectories of moving bubbles based on the center-of-gravity tracing algorithm. The bubbles were automatically detected by the luminance of the images, and the physical quantities of the bubble's motion and shape, such as velocity, size, and circularity, were measured in each scene of the video images. Consequently, the obtained variables not only enable us to investigate the qualitative features, but also the stochastic properties of the ascending behavior and shape change of the bubbles.

Bubble detection in the images from videos is shown in Fig. 5. The origin of the image analysis is placed at the bottom-left corner of each image. Following the coordinates for simulations, u_i ($i = 1, 2$ for u, w) denotes the velocity component [m/s] in the x_i direction ($i = 1, 2$ for x: horizontal, z: vertical). The other variables directly measured by the image analysis software were the bubble size (*i.e.*, the projected area of the bubble on the xz-plane) S, circumference L, circularity C, and maximum diameter of the bubble $d_{\max}$. The observation time for conducting image analysis was 10 s for Site-A, Case-1, Case-2, and Case-3; and 3.2 s for Site-B. The duration of bubble detection is significantly different for each bubble. Therefore, the analyzed data in the following sections were elaborately selected from the raw data, considering whether the detection time duration was long enough to conduct image analysis. As a result, the total number of bubbles analyzed under each condition was 167 for Site-A, 29 for Site-B, 101 for Case-1, 58 for Case-2, and 132 for Case-3.

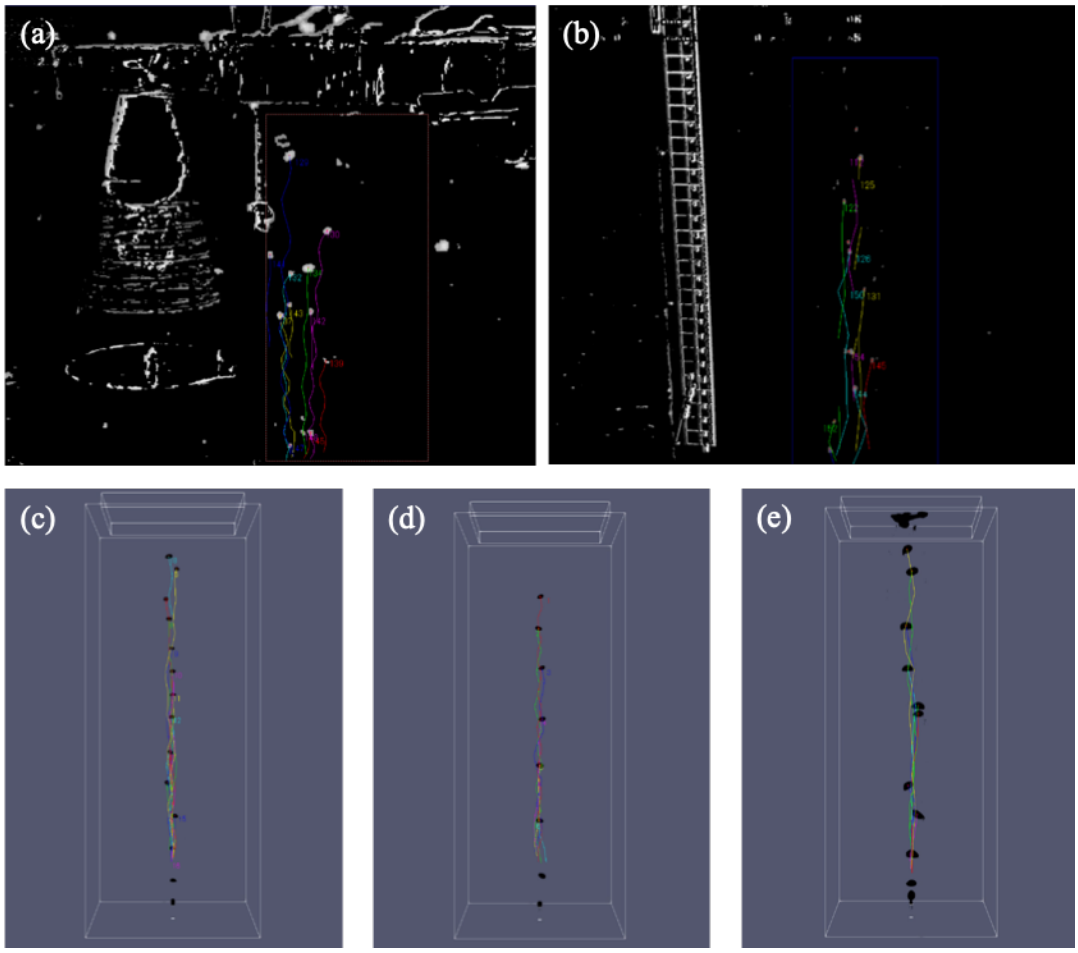

Figure 5. Bubble detection using images from videos of (a) Site-A, (b) Site-B, (c) Case-1, (d) Case-2, and (e

4. Data Validation

In this section, the validity of in-situ data at Site-A and Site-B, and the simulation results in Case-1, Case-2, and Case-3 were confirmed based on comparisons with previous studies. Fig. 6 shows the correlations between the mean equivalent bubble diameter $\overline{d_e}$ [m] and the mean vertical velocity $\overline{w}$ [m/s] of each bubble in (a) Site-A, (b) Site-B, (c) Case-1, (d) Case-2, and (e) Case-3. Here, the overbar indicates the operation averaging over the observation time of each bubble. As bubbles are typically ellipsoidal, d_e is calculated by $d_e = \left(\frac{6V}{\pi}\right)^{\frac{1}{3}}$. V [m^3] is the volume of the bubble, identified as $V = \frac{4}{3}$ abc $= \frac{2}{3}Sd_{\max}$, where a and b are the major and minor ellipsoid axes in the xz-plane, respectively, and c is the other ellipsoid axis assumed to be the same as a $(= \frac{d_{\max}}{2})$. The solid

line indicates the theoretical profile of terminal velocity U_t [m/s] for gas bubbles derived using the following equation (Lehrer et al., 1976), which considers the effect of viscosity on bubble motion as negligible.

$$U_t = \sqrt{3\frac{\sigma}{\rho_L d_e} + 0.5\frac{g d_e(\rho_L - \rho_b)}{\rho_L}}. \quad (8)$$

The dotted line shows the semi-empirical formula of U_t for MH bubbles, expressed as Eq. (9), which was confirmed by Sato et al. (2013), who examined the motion of a single MH bubble in a quiescent fluid.

$$U_t = \sqrt{2.68\frac{\sigma}{\rho_L d_e} + 0.42\frac{g d_e(\rho_L - \rho_b)}{\rho_L}}. \quad (9)$$

Here, g [m/s2] is gravity and ρ_b [kg/m3] is the bubble density defined in Eq. (10) or (11), in accordance with the bubble phase (Eqs. (10) and (11) were utilized for the gas and MH bubbles, respectively).

$$\rho_b = \rho_G, \quad (10)$$

$$\rho_b = \frac{V_H \rho_H + (V - V_H)\rho_G}{V}, \quad (11)$$

where V_H [m^3] is the volume of hydrate obtained by assuming a thickness of 90 μm for the hydrate layer (Sato et al. 2013) and ρ_H(=910) [kg/m^3] is the MH density reported by Soave (1972). The physical properties used to calculate Eqs. (8) and (11) are provided in Tables 1 and 2, respectively. As shown in Fig. 6 (a), (c), and (d), $\overline{w}$ at Site-A, Case-1, and Case-2 is very consistent with the theoretical and semi-empirical equations. $\overline{w}$ at Site-A shows an increasing trend in accordance with the increase in $\overline{d_e}$, which is a similar feature to MH bubbles (i.e., the dotted line); however, such trend is not observed in Case-1 and Case-2 as the variety of $\overline{d_e}$ is poor in those cases owing to the steady inlet condition employing a relatively small flow rate. However, $\overline{w}$ at Site-B and Case-3 tend to be larger than that of the referring equations. For Site-B, the differences between the profiles and the obtained data could be caused by the plume, namely the gas lift effect, as highlighted by Wang et al. (2016). For Case-3, the difference might be due to the acceleration of $\overline{w}$, whose flow rate is ten times larger than that of other simulation cases, owing to the upward flow generated by a swarm of bubbles. Overall, the fact that $\overline{w}$ is larger at Site-B than Site-A, and larger in Case-2 than Case-1 is consistent with the features of the profiles that U_t of an MH bubble is always greater than that of a gas bubble when d_e is the same.

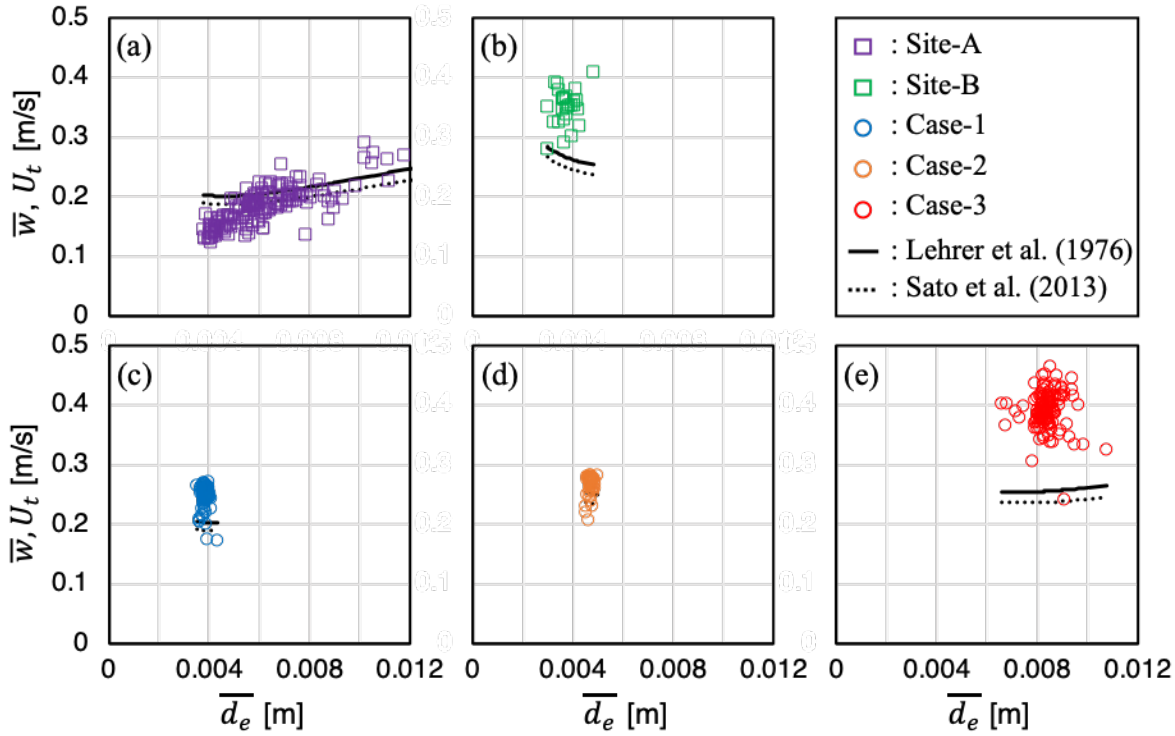

Figure 6. Correlations between mean equivalent diameter $\overline{d_e}$ [m] and mean vertical velocity $\overline{w}$ [m/s] of each

Table 2. Physical properties at Site-A and Site-B.

Site	Bubble state	Density (Water)	Density (Gas)	Viscosity (Water)	Viscosity (Gas)	Surface tension coefficient
		ρ_L [kg/m^3]	ρ_G [kg/m^3]	μ_L [Pa·s]	μ_G [Pa·s]	σ [N/m]
A	Gas & MH			$\times 10^{-3}$	$\times 10^{-5}$	
B	Gas			$\times 10^{-3}$	$\times 10^{-5}$	

The correlations between the ensemble average of the equivalent diameter $\langle\overline{d_e}\rangle$ [m] and amplitude of the bubble trajectory $\langle\overline{A}\rangle$ [m], and $\langle\overline{d_e}\rangle$ and frequency $\langle\overline{f}\rangle$ [Hz] are shown in Fig. 7 (a) and (b), respectively. Here, the angle brackets denote the average of all detected bubbles. A and f were obtained by identifying

the positions of both terminals in each zigzag motion. In Fig. 7 (a), besides the result at Site-B, a positive correlation was found between $\langle \overline{d_e} \rangle$ and $\langle \overline{A} \rangle$, aligning with the results of Sato et al. (2013). As the number of data samples (13 samplings) might not be sufficient due to the shorter observation period at Site-B relative to other conditions, the reliability of the result at Site-B could be waned. On the other hand, $\langle \overline{f} \rangle$ in all conditions ranges from 5–7 Hz, irrespective of $\langle \overline{d_e} \rangle$. This trend is consistent with that of Saffman (1956), who reported that the frequency of the zigzag motion is approximately 7 Hz and is independent of the size of the bubble. Fig. 7(c) and (d) show the Strhouhal number S_t ($= \langle \overline{f} \rangle \langle \overline{d_{\max}} \rangle / \langle \overline{w} \rangle$) and drag coefficient C_D ($= \frac{\rho_w g V - g(\rho_G V_G + \rho_H V_H)}{\frac{1}{2}\rho_w U^2 S}$) as a function of the Reynolds number R_e ($= \langle \overline{w} \rangle \langle \overline{d_{\max}} \rangle \rho_L / \mu_L$), respectively. The dotted line in Fig. 7(c) shows the profile of the MH bubbles obtained by Sato et al. (2013). The solid line in Fig. 7 (d) indicates the profile for water drops in air by Clift et al. (2005). As shown in Fig. 7 (c), S_t in all conditions is almost the same as that of the Karman vortex street of approximately 0.2 when $R_e < 2.0 \times 10^5$, which is consistent with the result of Sato et al. (2013). This tendency indicates that the zigzag motion is caused by the interaction between the oscillating wake and the instability of the motion of oblate bubbles, as revealed by numerous researchers (*e.g.*, Saffman (1956)). Moreover, as shown in Fig. 7 (d), C_D in all conditions is located on or above the solid line as bubbles in pure water and contaminated water must have greater C_D values than a rigid bubble when $R_e > 1.0 \times 10^3$(Gauden (1957)). For Site A, C_D is the largest among the other conditions in this study; this is because both the effects from the hydrate layer cause the suppression of the circulating inner flow and the oblate shape of the bubbles, leading to an increase in C_D at Site-A. As a result, the data obtained in this study are reasonable enough to analyze the statistical and stochastic features in the motion and shape of bubbles with and without the MH layer.

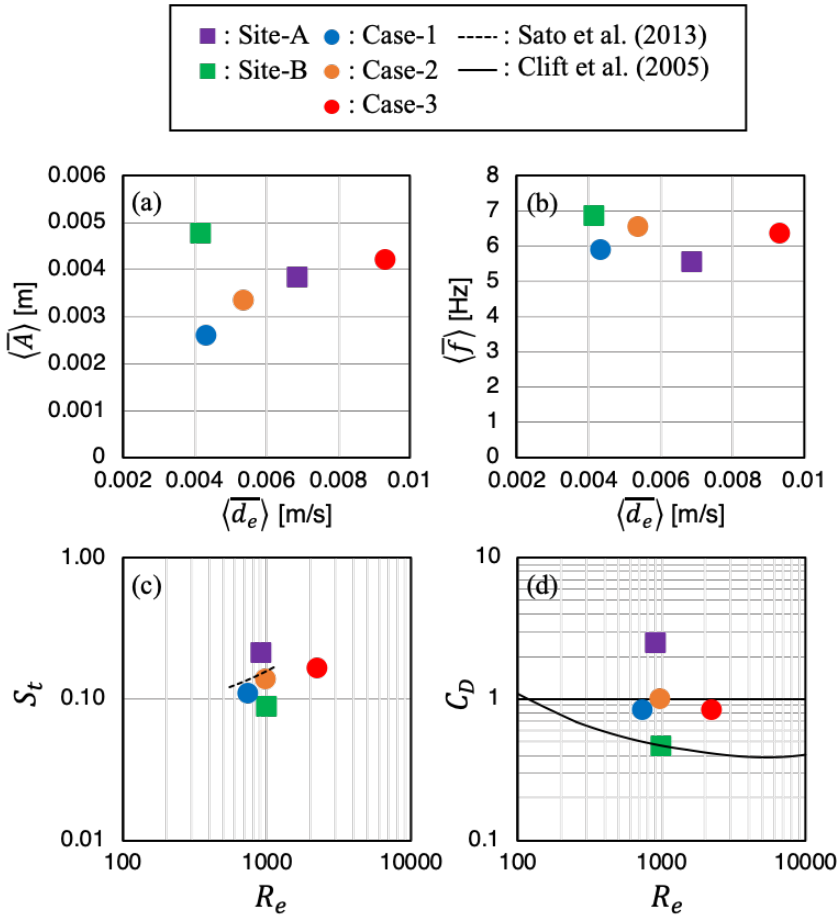

Figure 7. Correlations between ensemble average of (a) equivalent diameter $\langle \overline{d_e} \rangle$ [m] and amplitude of bubb

5. Statistical Features of Methane Bubble Motion and Shape

5.1 Comparisons of the Time Series Data and Statistics of a Bubble in Each Condition

One bubble was randomly selected from each condition to understand the basic behavior of an ascending bubble based on instantaneous and time-averaged data. Fig. 8 shows the relationships between the locations $\tilde{x}$ and $\tilde{y}$ [cm] and the residence time $\tilde{t}$ [s] in (a) Site-A, (b) Site-B, (c) Case-1, (d) Case-2, and (e) Case-3. For a certain variable ϕ, $\tilde{\phi}$ indicates the value standardized by its initial value ϕ_{ini}, as defined in Eq. (12).

$$\tilde{\phi} = \phi - \phi_{\mathrm{ini}}. \quad (12)$$

The standard deviation of $\tilde{x}$; $\sigma_{\tilde{x}}$ [cm] is also provided. As confirmed by the smooth increasing trend of $\tilde{y}$, bubbles were fairly detected in each condition. Although the trend of $\tilde{x}$ in Case-3 (Fig. 8 (e)) was subtle and the fluctuation of $\tilde{x}$ increased as the bubble ascended, those in other conditions clearly exhibited a zigzag motion, which is widely reported as a typical feature of bubbles, either with or without a hydrate layer on their surface. Owing to the ocean current, the bubbles in-situ data significantly deviated in the horizontal direction, as observed in Fig. 8 (a) and (b), which results in greater $\sigma_{\tilde{x}}$ at Site-A and Site-B.

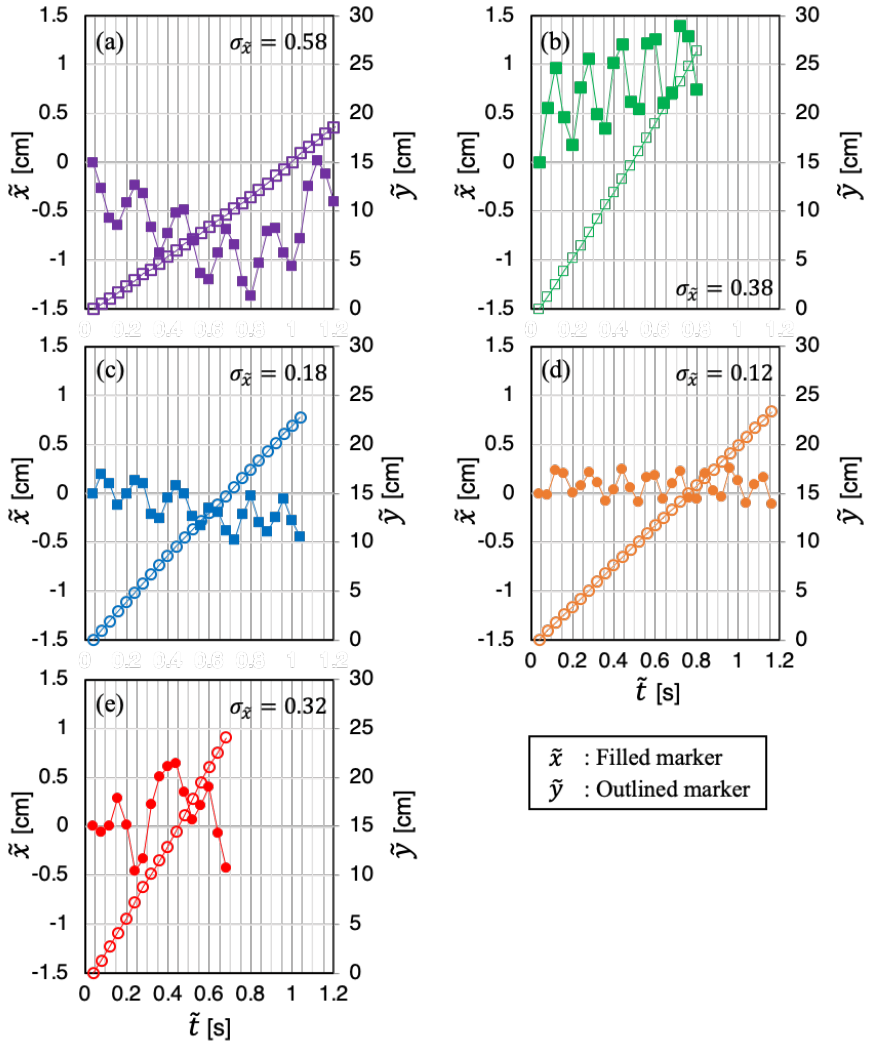

Figure 8. Correlations between locations $\tilde{x}$ and $\tilde{y}$ [cm], and residence time $\tilde{t}$ [s] of a bubble in (a) Site-A, (b)

Referring to the shape of the bubbles, the relationships between the bubble size S [cm^2], circularity C [-], and residence time $\tilde{t}$ are shown in Fig. 9. Here, C is calculated using Eq. (13):

$$C = \frac{4\,\mathrm{S}}{L^2}, \quad (13)$$

where L denotes the bubble circumference. Comparing $\overline{S}$ in each condition, the bubbles in Site-B, Case-1, and Case-2 are almost of the same size, whereas the bubbles in Site-A and Case-3 are markedly larger. Case-3 might display this trend as the inflow rate in Case-3 is ten times as much as that in Case-1 and Case-2. In addition, the decreasing trend of S in Case-3 was caused by the disruption of such relatively large bubbles owing to the greater distorting force. However, an increasing trend of S was only observed at Site-A. This result might be caused by the ocean current approaching the camera filming the bubbles at Site A; therefore, the resultant errors in S on the image analysis cannot be avoided in the current single-camera view, as highlighted by Wang and Socolosky (2015). Moreover, error values in C exceeding 1 can be observed, particularly in Fig. 9 (a) and (b), and could also be caused by the limitation of the situ-filming single-camera system, despite attempts to improve the visibility of bubbles at Site-B by utilizing the black panel (in Fig. 3 (b)) to provide a uniform background for post-image processing. In addition, the general features of C were found to exhibit a decreasing trend as S increases. Focusing on the differences between Case-1 (Fig. 9(c)) and Case-2(Fig. 9(d)), which can be understood based on the existence of the MH layer on the bubble surface, S in Case-1 tends to be smaller than that in Case-2, while C in both cases is almost the same.

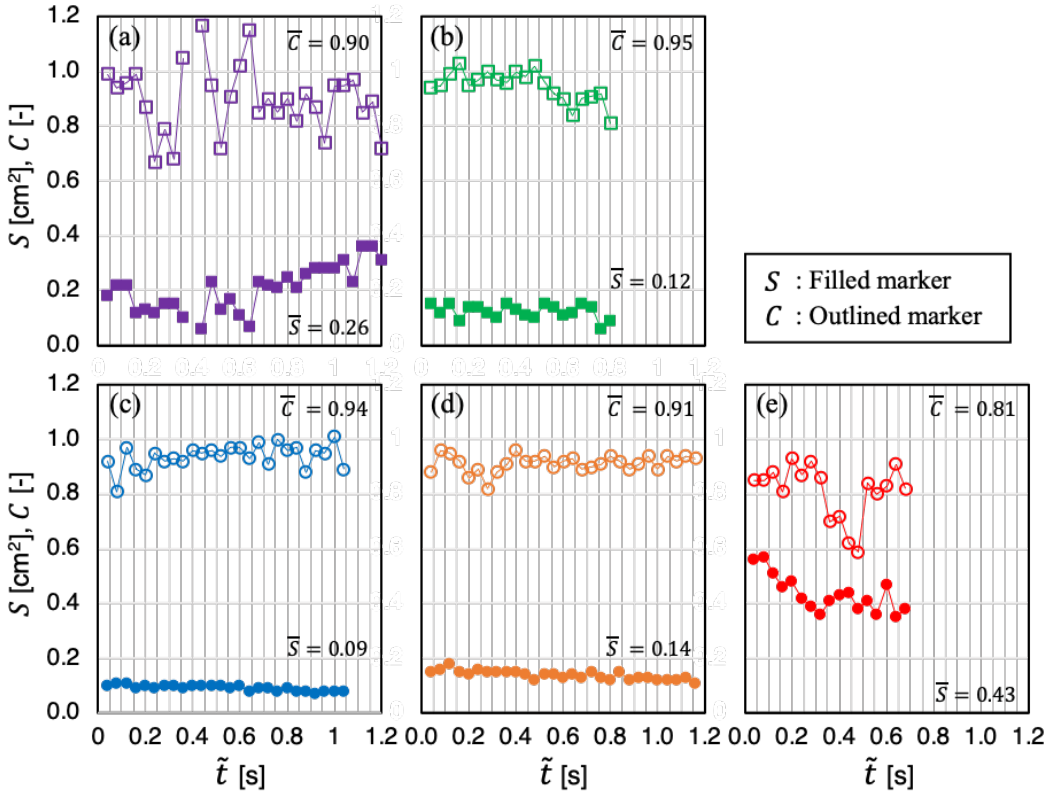

Figure 9. Correlations between the bubble size S [cm2] and circularity C [-], and residence time $\tilde{t}$ [s] of a bu

Fig. 10 shows the correlations between the instantaneous velocities u and w [cm/s] and the residence time $\tilde{t}$ of a bubble in each condition. The horizontal and vertical velocities averaged over the detected duration of each bubble, $\overline{u}$ and $\overline{w}$ [cm/s], are shown in each figure. Despite the greater deviations of $\tilde{x}$ in Site-A and Site-B (Fig. 8 (a) and (b)), $\overline{u}$ in all conditions was remarkably small (less than 1.0 cm/s), leading to no preference for directivity in the horizontal direction in any condition. On the other hand, w in Site-B is obviously larger than that in Site-A, while almost no difference in w exists between Case-1 and Case-2, whose inflow rates are the same, similar to the trends of $\overline{w}$ in Fig. 6. Accordingly, the difference in w at Site-A and Site-B is caused by the type of plume (i.e., blowout flare or natural sheep) rather than the formation of the MH layer. In addition, w in Case-3 was markedly greater than that in the other simulation cases, as observed for $\overline{w}$ in Fig. 6. As the zigzag motion is not clearly observed in Case-3 (Fig. 8 (e)), the time series variations of u and w were scattered as the size of the gas bubble increased. The time series data revealed differences in the shape and motion of the ascending bubbles in each condition

caused by the formation of the MH layer and ambient conditions, such as the gas flow rate, resultant bubble size, and velocity of the surrounding fluid.

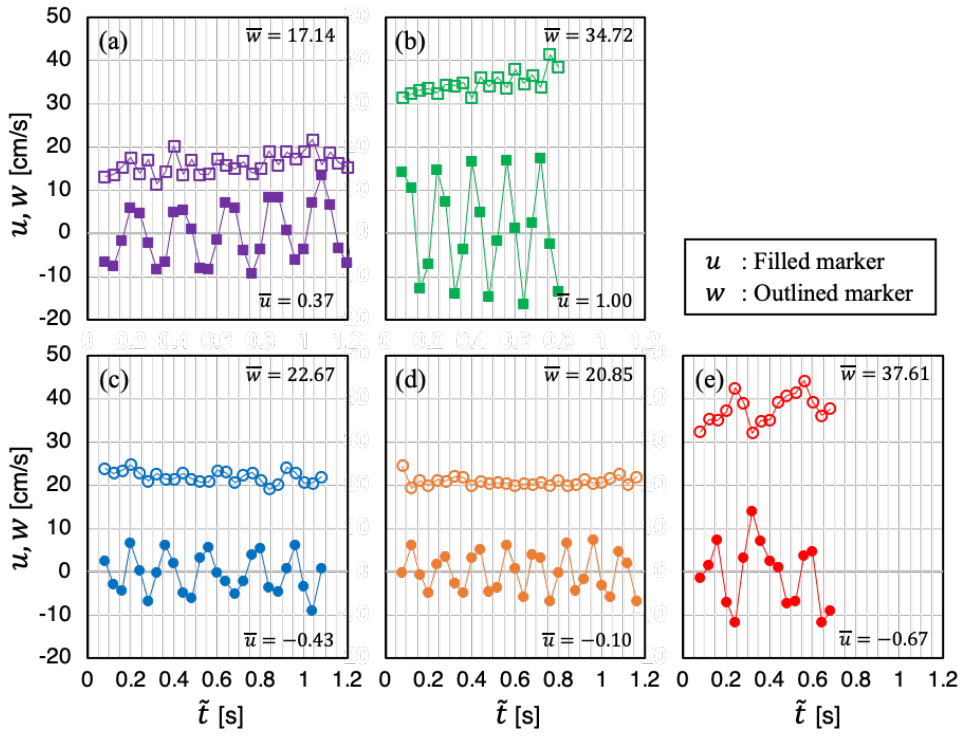

Figure 10. Correlations between instantaneous velocity u and w [cm/s], and residence time $\tilde{t}$ [s] of a bubble

5.2 Variety of the Motion and Shape of Ascending Bubbles

In this section, the statistical features of the bubble behavior in proportion to height z are revealed based on the average and deviation of variables in height ranges every 5 cm above $z_{\min}$ [cm]. Here, $z_{\min}$ represents the lowest height among the heights at which each bubble is first detected in each condition. As the number of sampling data points at Site B was insufficient, the following analysis was conducted only at Site-A, Case-1, Case-2, and Case-3. Fig. 11 shows the correlations of (a) mean location in the horizontal direction $\overline{\tilde{x}}$ [cm], mean bubble size $\overline{S}$ [cm^2], mean vertical velocity $\overline{w}$ [cm/s], and mean circularity $\overline{C}$, to mean height $\overline{z}$ [cm] in each height range of 5 cm. Here, the overbar indicates the ensemble average of the variables in height ranges every 5 cm above $z_{\min}$ [cm]. The error bars indicate the standard deviation of the variables ϕ; σ_ϕ. As observed in Fig. 11(a), $\overline{\tilde{x}}$ at Site-A alone clearly showed an increasing trend in accordance with height. As $\sigma_{\tilde{x}}$ displayed a similar tendency to $\overline{\tilde{x}}$, the

results at Site A were considered to be affected by the unsteady ocean current running to the right-hand side of the image, as shown in Fig. 8 (a). As $\sigma_{\tilde{x}}$ in the simulation cases also slightly increases with height, the trajectory of the bubble diverges as the bubble increases, irrespective of the formation of the MH layer. $\overline{S}$ at Site-A also increased with height above 10 cm, which indicates that the ocean current approached the filming camera, as mentioned earlier. The relatively large values of $\sigma_{\overline{S}}$ implies some of the bubbles at Site A were affected by the intermittent ocean current. On the other hand, the results obtained by the simulations show quite small variations in $\overline{\tilde{x}}$ in all cases and a slight decrease in $\overline{S}$ in Case-3 in accordance with the increase in $\overline{z}$. These trends are consistent with the data presented in Figs. 8 and 9. Therefore, these facts paradoxically confirm the representativeness of the bubbles whose time-series data are presented in the previous section. The profiles of $\overline{w}$ at Site-A and Case-3 show a similar increasing trend with $\overline{z}$ in Fig. 11 (c), while the average of $\overline{w}$ in Case-3 is apparently greater than that at Site A. As $\overline{S}$ above 15 cm at Site-A and Case-3 might be in the same range (based on $\sigma_{\overline{S}}$), despite consideration of the parallax error of the current single-camera system at Site-A, gas bubbles have a higher rising speed than MH bubbles when the bubble size is the same. This trend is consistent with the features of the theoretical profiles in Fig. 6 and the results of Case-1 and Case-2 in Fig. 11 (c). Furthermore, as shown in Fig. 11 (b) and (d), smaller bubbles tend to have larger $\overline{C}$ while MH bubbles might have larger $\overline{C}$ rather than gas bubbles. These features are due to the greater resistance of the small bubbles and MH bubbles against the distorting force exerted by the surrounding fluid.

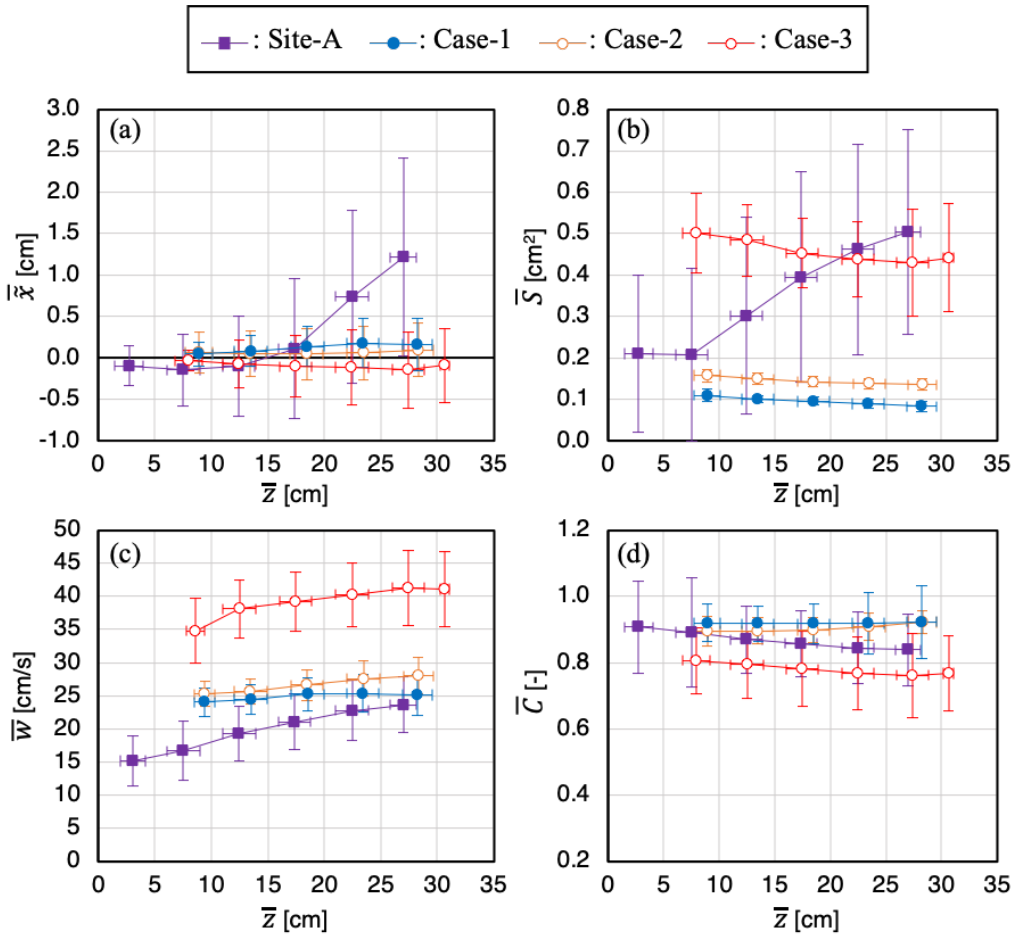

Figure 11. Correlations of (a) mean location in the horizontal direction $\overline{\tilde{x}}$ [cm], (b) mean bubble size $\overline{S}$ [cm^2

6. Stochastic Features in Bubble Motion

6.1 Probability Density Function

As the behavior of ascending bubbles is unsteady owing to fluctuations in the ambient environment and formation of the MH layer, it is important to understand their temporal variations. In this section, the stochastic features of bubble behavior are discussed. Fig. 12 shows the probability density functions (PDFs) of $f(\phi)$ as a function of the normalized random variables $\phi = (\varphi - \langle\overline{\varphi}\rangle)/\sigma_\varphi$, where φ is the (a) location in the horizontal direction $\tilde{x}$, (b) vertical velocity w, or (c) bubble size S in each figure. The black dotted line indicates the Gaussian distribution. In Fig. 12 (a), only $f(\phi)$ at Site-A has a negatively skewed distribution, indicating an ocean current at Site-A, which is consistent with the

increasing trend of $\overline{\widetilde{x}}$ with height in Fig. 11 (a). However, other simulation cases tend to follow a Gaussian distribution, which indicates that most of the bubbles might maintain a zigzag motion perpendicularly. This feature is illustrated in Fig. 11 (a). Accordingly, there was no obvious tendency for ascending bubbles to prefer any direction, irrespective of the formation of the MH layer. In Fig. 12 (b), all distributions are similar to each other, and shows a slight shift to the negative side on the horizontal axis compared to the Gaussian distribution. However, w can be assumed to be predicted by the Gaussian distribution, regardless of the conditions in this study. In Fig. 12 (c), the distributions of S at Site-A and Case-1, which are the results for MH bubbles, have a distinct peak at $\phi = -1.0$ and -0.4, respectively, while those at Case-2 and Case-3 basically follow the Gaussian distribution, despite a slight shift to the negative side in the horizontal axis. This trend indicates that the MH bubbles have some predilections for their size controlled by the generated hydrate layer. On the contrary, the gas bubbles in Case-2 and Case-3 were more diverged in size compared to the MH bubbles.

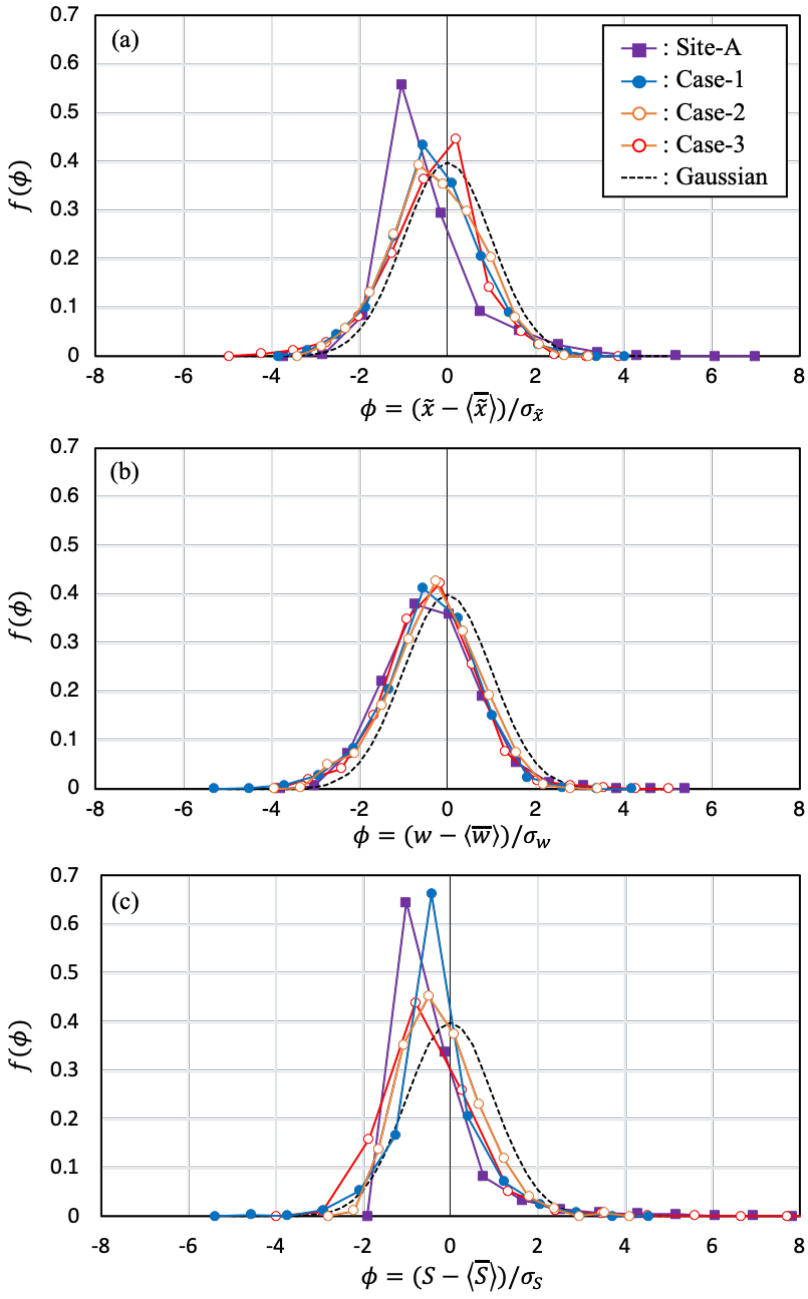

Figure 12. Probability density functions of (a) location in the horizontal direction $\tilde{x}$, (b) vertical velocity w,

6.2 Joint Probability Distributions

As the differences in bubble size are recognized in the previous section, the joint probability distributions (JPDs) of variables in relation to the bubble shape were examined. Fig. 13 shows the JPDs referring to S and C at (a) Site-A, (b) Case-1, (c) Case-2, and (d) Case-3. As shown in Fig. 13 (a), a negative correlation tends to be observed when $\phi_1 < 0$ and $\phi_2 > 0$; however, the correlation disappears as ϕ_1 becomes large. As this trend can be somewhat recognized in Fig. 13 (b), the distortion of the MH bubbles whose surfaces are rigid due to the hydrate layer is restricted, which results in C being uniquely determined upon the provision of S. The trend was more apparent when the bubble size was small. However, Figs. 13 (c) and (d) show wide distributions, indicating the absence of a certain relationship between S and C for gas bubbles.

This trend is observed in Fig. 14, which shows the JPDs for S and L. The positive correlation was clearly observed at site A. Although a similar trend can be observed in Case-1, the wider distributions in the simulations indicate that the variation in the bubble shape is enriched in the simulation rather than the survey, which can be attributed to the differences in surface tension in the survey and simulation. Considering all results presented in Section 5, the differences in surface tension could lead to significant differences in bubble growth in terms of size and distorting features.

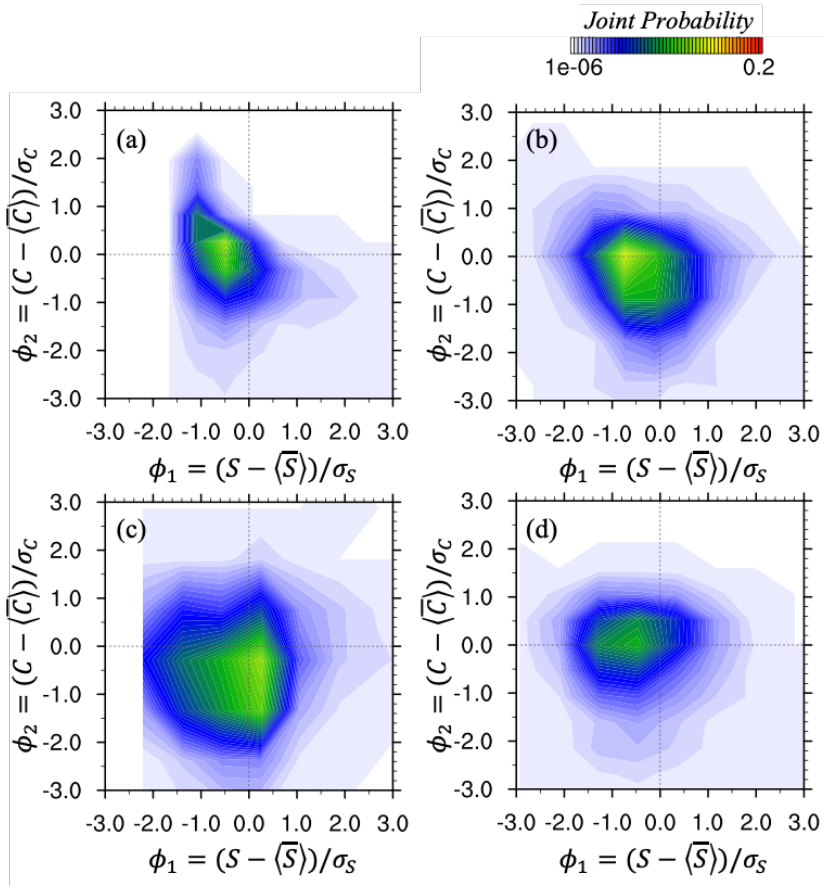

Figure 13. Joint probability distributions referring to bubble size S and circularity C at (a) Site-A, (b) Case

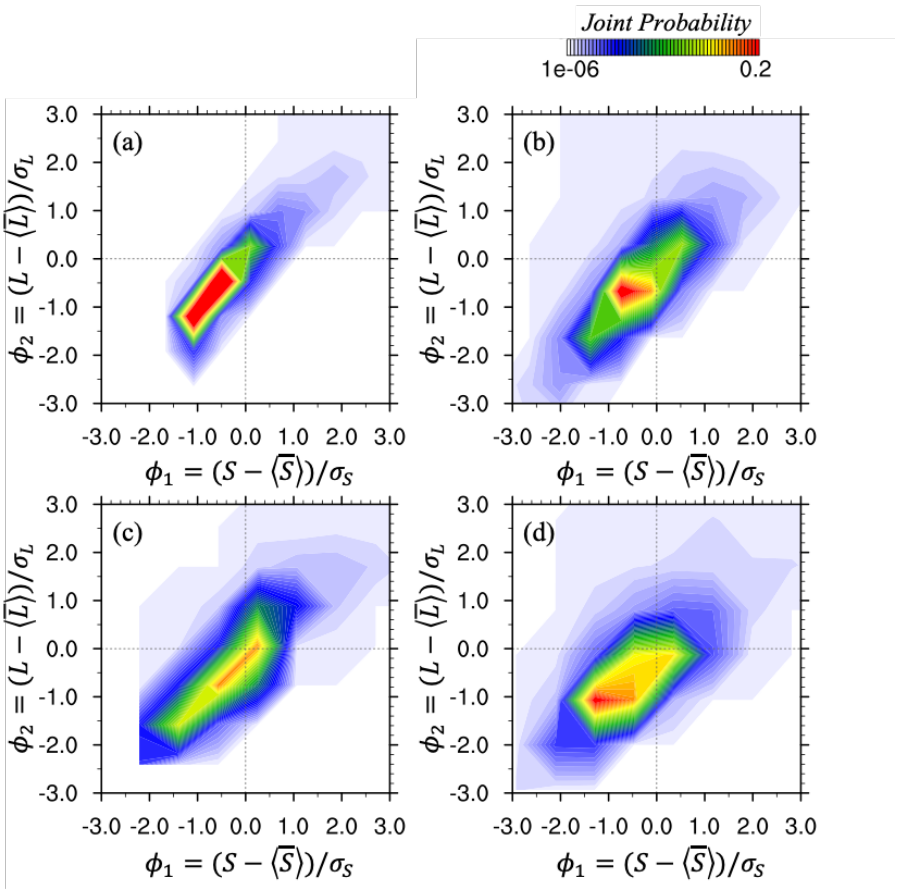

Figure 14. Joint probability distributions referring to bubble size S and circumference L at (a) Site-A, (b) C

7 Conclusions

In this study, statistical and stochastic features referring to the motion and shape of ascending methane bubbles, including the effect of the MH layer on the bubble surface, were investigated using two-dimensional image analysis. Video images were collected in the Sea of Japan, offshore Niigata prefecture, and via numerical simulations.

The vertical velocity of the gas bubbles tended to be larger than that of the MH bubbles when the bubble size was identical, aligning with the theoretical and semi-empirical equations for the cases with and without the MH layer. In addition, the tendencies of the equivalent diameter of bubbles, such as the increase in magnification of the amplitude of bubble motion and no effects on the frequency of bubble motion, were confirmed with both MH bubbles and gas bubbles. The Reynolds number, Strhouhal number, and drag coefficient of

the bubbles were sufficiently reasonable to analyze the statistical and stochastic features in ascending bubbles with and without an MH layer.

Regardless of the MH layer, most of the bubbles exhibited zigzag or spiral motion, and no preference for directivity in the horizontal direction was confirmed in any condition. Irrespective of the MH layer, smaller bubbles tended to have higher circularity, and the resistance against distortion was confirmed to be more abundant in smaller bubbles than in larger bubbles. Although parallax errors in the surveys were recognized in the current single-camera system, gas bubbles had a higher rising speed and smaller circularity than MH bubbles when the bubble size was identical.

The PDFs of the bubble position in the horizontal direction for the simulations tended to follow a Gaussian distribution, which indicated that most of the bubbles could maintain a zigzag motion perpendicularly. However, irrespective of the effect of the ocean current, the vertical velocity was predicted by the Gaussian distribution under all conditions. The PDF of the MH bubble size had a distinct peak at a smaller size than its average size, whereas those for the gas bubble size could obey the Gaussian distribution with a slight shift to the negative side in the horizontal axis. This finding implies that the MH bubbles have some predilections as their size is controlled by the hydrate skin. Based on the negative correlation observed in the JPDs with respect to the bubble size and circularity of the MH bubbles, the distortion of the MH bubbles whose surfaces were rigid owing to the MH layer was restricted. As a result, a stable value of circularity uniquely determined by the bubble size was realized for MH bubbles. In accordance with the JPDs of the bubble size and circumference, the variation in the bubble shape was enriched in the simulations rather than the survey, which can be attributed to the different treatment of surface tension in the simulations from that in the survey (*i.e.*, the reality).

Analysis of the video images obtained in ocean surveys and simulations provided a comprehensive view of the behavior of ascending bubbles with and without the MH layer. Although some discrepancies were recognized between them owing to the parallax error in surveys or the limited information for the simulations, it is still open to discuss the representativeness of the numerical procedure. More precise comparisons between the situ-data and simulation data are necessary to develop more accurate numerical models to reproduce the behavior of ascending MH bubbles, which will be the focus of our future work.

Acknowledgments

This study was supported as part of the methane hydrate research project funded by the Ministry of Economy, Trade, and Industry (METI). The authors are grateful for the data acquired in the ocean survey on June 9-13, 2019 and November 14–19, 2021 by the research vessel, "Kaiyo Maru No.1" (Kaiyo Engineering Co., Ltd.).

Open Research

The general-purpose fluid analysis code, NuFD/FrontFlowRed, used in this study was extended by Kyushu University (https://doi.org/10.1016/j.apt.2020.05.002). Ver. 8.6, two-dimensional motion analysis software Move-tr/2D (Library Co., Ltd.) is available via a private license.

References

Aoyama, C., & Maeda, N. (2021), Proposed Methodology to Quantify the Amount of Methane Seepage by Understanding the Correlation Between Methane Plumes and Originating Seeps. *Frontiers in Earth Science*, *9*, 1–6. doi:10.3389/feart.2021.589399

Aoyama, C., & Matsumoto, R. (2009), Acoustic Surveys of Methane Plumes by Quantitative Echo Sounder in Japan Sea and the Estimate of the Seeping Amount of the Methane Hydrate Bubbles. *Chigaku Zasshi (Jounal of Geography)*, *118*(1), 156–174. doi:10.5026/jgeography.118.156

Brackbill, J. U., Kothe, D. B., & Zemach, C. (1992), A continuum method for modeling surface tension. *Journal of Computational Physics*, *100*(2), 335–354. doi:10.1016/0021-9991(92)90240-Y

Davanipour, M., Javanmardi, H., & Goodarzi, N. (2018), Chaotic Self-Tuning PID Controller Based on Fuzzy Wavelet Neural Network Model. *Iranian Journal of Science and Technology - Transactions of Electrical Engineering*, *42*(3), 357–366. doi:10.1007/s40998-018-0069-1

Gaudin, A. M, (1957). Flotation. *McGraw Hill Inc.*, New York.

Kvenvolden, Keith A. (1993), Gas hydrates—geological perspective and global change. *Reviews of Geophysics*, 31(2), 173–187.

Lee, M. W. (2000), Gas hydrates amount estimated from acoustic logs at the Blake Ridge, Sites 994, 995, and 997. *Proceedings of the Ocean Drilling Program: Scientific Results*, *164*, 193–198. doi:10.2973/odp.proc.sr.164.239.2000

Lehrer, I. H. (1976), A Rational Terminal Velocity Equation for Bubbles and Drops at Intermediate and High Reynolds Numbers. *Journal of Chemical Engineering of Japan*, *9*(3), 237–240. doi:10.1252/jcej.9.237

Leifer, I., Luyendyk, B. P., Boles, J., & Clark, J. F. (2006), Natural marine seepage blowout: Contribution to atmospheric methane. *Global Biogeochemical Cycles*, *20*(3), 1–9. doi:10.1029/2005GB002668

Liu, C. S., Schnürle, P., Wang, Y., Chung, S. H., Chen, S. C., & Hsiuan, T. H. (2006), Distribution and characters of gas hydrate offshore of southwestern Taiwan. *Terrestrial, Atmospheric and Oceanic Sciences*, *17*(4), 615–644. doi:10.3319/TAO.2006.17.4.615(GH)

Matsumoto, R., Okuda, Y., Hiruta, A., Tomaru, H., Takeuchi, E., Sanno, R., et al. (2009), Formation and Collapse of Gas Hydrate Deposits in High Methane Flux Area of the Joetsu Basin, Eastern Margin of Japan Sea. *Chigaku Zasshi (Jounal of Geography)*, *118*(1), 43–71. doi:10.5026/jgeography.118.43

Matsumoto, R., Tomaru, H., & Lu, H. (2004), Detection and evaluation of gas hydrates in the Eastern Nankai Trough by geochemical and geophysical methods. *Resource Geology*, *54*(1), 53–67. doi:10.1111/j.1751-3928.2004.tb00187.x

Matsumoto, R. (2005), Methane plumes over a marine gas hydrate system in the eastern margin of Japan Sea : A possible mechanism for the transportation of subsurface methane to shallow waters. *Proceedings of the 5th International Conference on Gas Hydrates*, Trondheim, 749–754.

National Institute of Advanced Industrial Science and Technology. (2019), *Action Plan for Research and Development of Surface Type Methane Hydrate (FY2019-2022)*.

Roberts, H. H. (2001), Fluid and gas expulsion on the northern Gulf of Mexico Continental Slope: Mud-prone to mineral-prone responses. Natural Gas Hydrates: Occurrence, Distribution, and Detection edited by Paull, C. K. & Dillon, W. P. *Geophysical Monograph Series*, 124, AGU, 145–161. doi:10.1029/GM124p0145

Saffman, P. G. (1956), On the rise of small air bubbles in water. *Journal of Fluid Mechanics*, *1*(3), 249–275. doi:10.1017/S0022112056000159

Sato, Y., Kiyono, F., Ogasawara, K., Yamamoto, Y., Sato, T., Hirabayashi, S., & Shimizu, Y. (2013), An Experimental Study on the Dynamics of a Rising Methane Bubble Covered with Hydrates. *Journal of MMIJ*, *129*(4), 124–131. doi:10.2473/journalofmmij.129.124

Soave, G. (1972), Equilibrium constants from a modified Redlich-Kwong equation of state. *Chemical Engineering Science*, *27*(6), 1197–1203. doi:10.1016/0009-2509(72)80096-4

Versteeg, H. K., and Malalasekera, W. (1995), An Introduction to Computational Fluid Dynamics: The Finite Volume Method. *Pearson Education Limited*.

Wang, B., and Socolofsky, S. A. (2015), A deep-sea, high-speed, stereoscopic imaging system for in situ measurement of natural seep bubble and droplet characteristics. *Deep-Sea Research Part I: Oceanographic Research Papers*, *104*, 134–148. doi:10.1016/j.dsr.2015.08.001

Wang, B., S. A. Socolofsky, J. A. Breier, and J. S. Seewald (2016), Observations of bubbles in natural seep flares at MC 118 and GC 600 using in situ quantitative imaging, *J. Geophys. Res. Oceans*, 121, 2203–2230, doi:10.1002/ 2015JC011452.

Watanabe, H., and Kurose, R. (2020), Modeling and simulation of coal gasification on an entrained flow coal gasifier. *Advanced Powder Technology*, *31*(7), 2733–2741. doi:10.1016/j.apt.2020.05.002

Weller, H. G. (1993), The development of a new flame area combustion model using conditional averaging. *Thermo-Fluids Section Report TF/9307*, *9307*(March).